

# Fundamental Aspects of Enantioselective Heterogeneous Catalysis: the Surface Chemistry of Methyl Pyruvate on Pt{111}

Jonathan M. Bonello, Federico J. Williams, Ashok K. Santra, and Richard M. Lambert\*

Department of Chemistry, University of Cambridge, Lensfield Road, Cambridge CB2 1EW, England

Received: June 7, 2000; In Final Form: August 5, 2000

STM, NEXAFS, XPS, and TPR have been used to characterize the adsorption and reactivity of methyl pyruvate on Pt{111}. In the absence of coadsorbed hydrogen, methyl pyruvate polymerizes at room temperature yielding polymer chains, partly dendritic. The STM and XPS data provide independent estimates of the average length, found to be  $\sim 9$  monomer units. NEXAFS shows that this polymer contains C=O bonds and no C=C bonds; the C=O bonds are inclined at  $64^\circ \pm 5^\circ$  with respect to the metal surface. It is proposed that polymerization occurs by hydrogen elimination from the monomer, followed by an aldol condensation that involves elimination of methanol. This mechanism is in excellent accord with the intramolecular bonding, shape, and reactivity of the polymer deduced from the NEXAFS, STM, and TPR results. Coadsorbed hydrogen completely suppresses polymerization. These findings suggest that irreversible deactivation during start-up or steady-state operation of Pt catalysts during enantioselective hydrogenation of alkyl pyruvates can be due to hydrogen starvation which results in polymerization of the prochiral reactant.

## 1. Introduction

Although enantioselective heterogeneous catalysts are rarities, their potential importance is huge because the reactions are almost enzymatic in specificity. Chiral heterogeneous catalysis is of leading importance in current chemical research and is a subject of increasing interest in both the academic and industrial communities as judged by the number of papers, reviews, and books on every aspect of the field.<sup>1–4</sup> However, even though the number of known systems is increasing, the subject as a whole remains at a relatively early stage of development. This is especially true in regard to fundamental studies of the surface phenomena involved, even in the case of the most studied reactions.

Only two classes of reactions have been extensively studied and well documented. These are the asymmetric hydrogenation of 2-alkanones and  $\beta$ -ketoesters in solution over nickel catalysts modified by tartaric acid<sup>4–6</sup> and  $\alpha$ -ketoester hydrogenation in solution over platinum catalysts modified by chiral cinchona alkaloids. In these systems a chiral adsorbate is used to impart chirality to an intrinsically achiral metal surface: the resulting chiral adsorption sites are believed to act as the centers for an enantioselective reaction. In both cases, high enantiomeric excesses (ee) of up to 90–95% can be achieved. However, this is only the case for a limited number of reactant types, as discussed below. Moreover, clear hypotheses have emerged only in the case of  $\alpha$ -ketoester hydrogenation over platinum surfaces. Consequently, several mechanistic models have been proposed recently,<sup>3,7–10</sup> although all are limited by the need to make assumptions regarding the adsorption mode of the reactant and the modifier involved.

The prototypical reaction involving hydrogenation of methyl pyruvate is illustrated in Figure 1. It proceeds efficiently on Pt particles at room temperature. Depending on whether the Pt surface is modified by cinchonidine or cinchonine (its near enantiomer) (*R*)- or (*S*)-methyl lactate are produced, respectively,

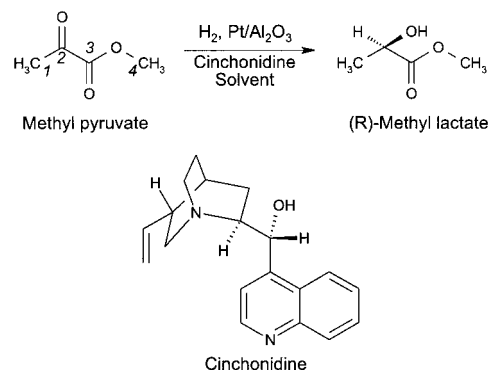


**Figure 1.** Reaction scheme for the enantioselective hydrogenation of methyl pyruvate in solution over a cinchonidine-modified Pt/Al<sub>2</sub>O<sub>3</sub> catalyst.

in enantiomeric excess. This reaction was first reported in 1979 by Orito et al.,<sup>11,12</sup> whose findings prompted further work by several groups.<sup>13–16</sup> Even so, there have been very few direct observations on relevant surface species.<sup>14,17–19</sup>

Development of a realistic mechanistic model calls for the explanation of a number of characteristic features of the reaction. The information required for construction of such a model includes knowledge of the surface chemistry and structure of the reactant. Here we report results from the first detailed study of the reactant, methyl pyruvate, on the Pt{111} surface. This surface was chosen because in practice it is found that the enantioselective reaction proceeds only on Pt particles whose size exceeds 3 nm,<sup>20,21</sup> suggesting that the low index planes of the metal dominate its useful catalytic behavior. The molecular orientation of surface species and their spatial distribution and reactivity in the presence and absence of hydrogen has been determined by a combination of NEXAFS, XPS, STM, and TPR.

## 2. Experimental Methods

NEXAFS spectra at the carbon K-edge were acquired in partial electron yield mode on beamline 1.1 at the Daresbury

\* Corresponding author E-mail: RML1@CAM.AC.UK. Tel: +44 1223 33 64 67. Fax: +44 1223 33 63 62.

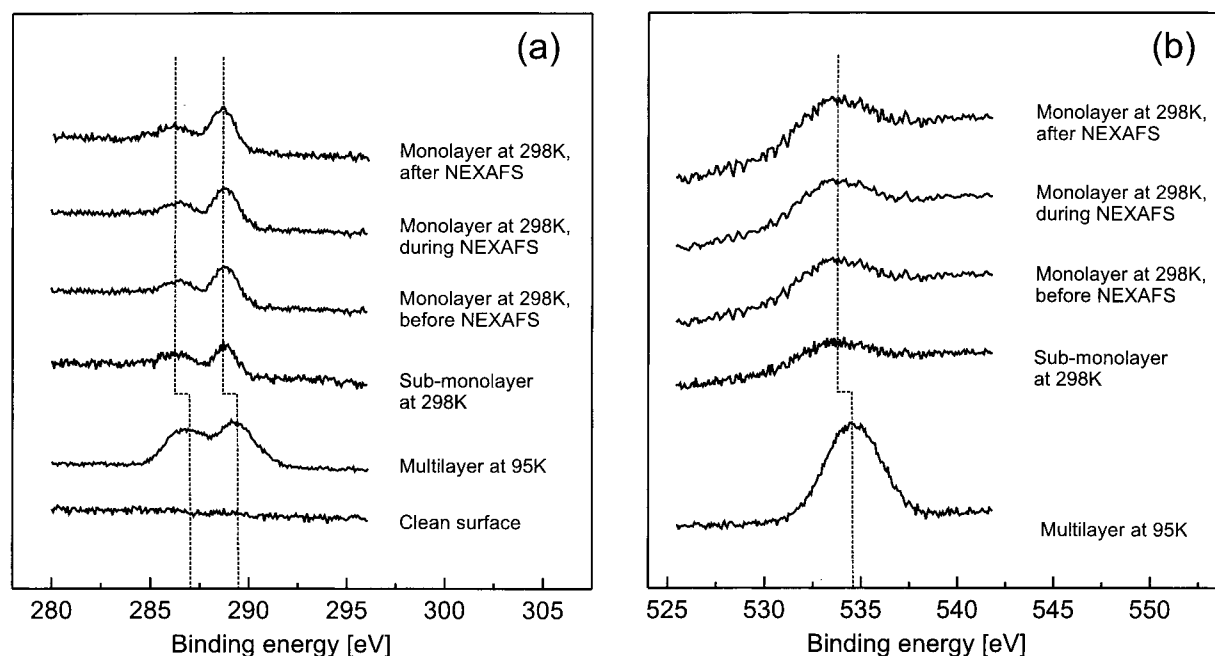


**Figure 2.** (a) Carbon (1s) XP spectra for a methyl pyruvate multilayer at 95 K and monolayer at 298 K on Pt{111}. All spectra were recorded at a photon energy of 500 eV with the incident beam normal to the surface. (b) Oxygen (1s) XP spectra for a methyl pyruvate multilayer at 95 K and monolayer at 298 K on Pt{111}. All spectra were recorded at a photon energy of 750 eV with the incident beam normal to the surface.

Synchrotron Radiation Source. The end chamber incorporated a hemispherical electron energy analyzer, liquid nitrogen-cooled sample manipulator, quadrupole mass spectrometer, and LEED optics. Energy calibration of the monochromators was carried out at the carbon edge by monitoring the absorption features due to weak carbon contamination (284.7 eV) of the optics in the spectrum of the Au mesh and was found to be consistent to  $\pm 0.5$  eV. The photon energy resolution at the carbon K-edge was 0.5 eV and the degree of linear polarization is estimated as 95%.<sup>22</sup> NEXAFS spectra were recorded at several angles between normal ( $\theta = 90^\circ$ ) and grazing ( $\theta = 20^\circ$ ) incidence. The system base pressure during capillary dosing of methyl pyruvate and during spectral acquisition was  $\sim 1 \times 10^{-10}$  Torr.

XPS measurements were carried out using the linearly polarized soft X-ray beam and binding energies were calibrated against the Pt (4f)<sub>7/2</sub> peak at 71.2 eV.<sup>23</sup> Surface concentrations of adsorbed species and stoichiometric ratios were determined from the integrated intensities of the adsorbate and substrate core level lines using standard methods.<sup>24</sup>

The Pt{111} crystal, cut within  $0.5^\circ$  of the (111) orientation, was cleaned by argon ion sputtering (1 keV) followed by annealing under vacuum at 1100 K. XPS and LEED were used to check the surface cleanliness and long range order, respectively. High purity methyl pyruvate (MP, Fluka, purum. >97%) was freshly distilled under vacuum and subsequently subjected to several freeze–pump–thaw cycles. After conditioning the gas delivery system with methyl pyruvate, the adsorbate was introduced into the chamber where its purity was monitored by mass spectrometry.

STM experiments were carried out using an Omicron UHV STM-1 instrument (base pressure  $5 \times 10^{-11}$  mbar) described elsewhere.<sup>25</sup> This apparatus incorporated LEED/Auger facilities used for surface characterization prior to adsorption experiments. Images were acquired in constant current mode. Control experiments indicated that there were no tip-induced artifacts such as molecular displacements or adsorbate decomposition. TPR spectra were obtained in a UHV chamber equipped with LEED/Auger facilities and a quadrupole mass spectrometer. The

latter was fitted with a collimator and the crystal could be positioned at a distance of approximately 10 mm from the collimator aperture. Detection was therefore limited to species desorbing from the center of the front face of the crystal. Desorption data were corrected for instrumental sensitivity and the linear sample heating rate was  $10 \text{ K} \cdot \text{s}^{-1}$ .

### 3. Results and Discussion

**3.1. X-ray Photoelectron Spectroscopy.** C(1s) and O(1s) multilayer XP spectra were acquired to assist with the interpretation of the monolayer spectra. Multilayer spectra taken at 95 K for both core levels after exposing the clean Pt{111} surface to 25L (1L = 1 Langmuir =  $10^{-6}$  Torr·s) are shown in Figure 2 (a) and (b). The thickness of the multilayer, estimated from the attenuation of the Pt(4f) signal, is  $\sim 10$  Å. The C(1s) multilayer spectrum shown in Figure 2(a) is characterized by two main contributions at 289.4 eV (fwhm = 2.27 eV) and 286.5 eV (fwhm = 2.53 eV). The former agrees well with the C(1s) binding energies associated with carbonyl functional group and the latter with the binding energy for alkyl carbon.<sup>26</sup> The ratio of the normalized, integrated areas of the two carbon peaks,  $C_{\text{carbonyl}}:C_{\text{alkyl}}$ , in the C(1s) multilayer XP spectrum is 1:1, indicative of the presence of equal numbers of carbon atoms in similar chemical environments. This is in accord with the molecular structure of methyl pyruvate, which contains two carbon atoms in a carbonyl environment and two carbon atoms in an alkyl environment. However, it should be noted that in this regime of photoelectron kinetic energies, diffraction effects due to backscattering by the substrate can be significant and we did not examine the effect of varying the detection geometry. Our reported absolute intensities for any given condition are therefore subject to uncertainty. However, *changes* in relative intensities are certainly significant and may be taken at face value when drawing qualitative conclusions.

The multilayer XP spectrum for O(1s) consists of a single broad peak which appeared at a binding energy of 534.6 eV with fwhm = 3.33 eV (Figure 2(b)). After correction for the carbon and oxygen atomic subshell cross-sections at the relevant

photon energy,<sup>27</sup> the C(1s) and O(1s) multilayer data yield a total carbon-to-oxygen ratio,  $C_{\text{total}}:O_{\text{total}}$ , of  $1.29 \pm 0.05$ . This is in good accord with the stoichiometric ratio of 1.33 for  $C_{\text{total}}:O_{\text{total}}$  in the methyl pyruvate molecule, suggesting that the adsorbate retained its integrity in the multilayer formed at 95 K.

The C(1s) and O(1s) submonolayer and monolayer XP spectra of pyruvate adsorbed at 298 K are also shown in Figure 2(a) and (b), respectively. Coverages were deduced from an XPS intensity versus exposure calibration curve acquired at room temperature. Under these conditions uptake ceases at the monolayer stage, thereby providing the required reference point. In both the submonolayer and monolayer regimes at 298 K the C(1s) XP spectra, shown in Figure 2(a), are characterized by two main features centered at 288.6 eV (fwhm = 1.53 eV) and 286.2 eV (fwhm = 1.58 eV), which coincide well with literature values for adsorption of similar molecules on Pt{111}.<sup>26</sup> That is, shifts toward lower binding energy by 0.8 eV and 0.3 eV respectively with respect to the corresponding emission from the multilayer. The O(1s) spectra for the submonolayer and the monolayer regimes at 298 K are shown in Figure 2(b). It is evident that both spectra show one rather broad peak centered at 533.6 eV (fwhm = 3.67 eV) and, similarly to the analogous C(1s) spectra, it is shifted by 1 eV toward lower binding energy with respect to the corresponding peak in the multilayer spectrum. In each case, the observed shifts could reflect the effect of increased extra-atomic relaxation around the core hole in the case of the chemisorbed layer, due to electrons in the metal.

The C(1s) and O(1s) signals for the submonolayer and monolayer cases were used to estimate the surface coverage of methyl pyruvate. The submonolayer spectrum corresponds to a surface coverage of  $1.7 \times 10^{14}$  carbon atoms·cm<sup>-2</sup> ( $\pm 5\%$ ) calculated from the C(1s) XPS data (Figure 2(a)). As each methyl pyruvate molecule contains four carbon atoms, this corresponds to a surface coverage of approximately  $4.25 \times 10^{13}$  molecules·cm<sup>-2</sup> ( $\pm 5\%$ ). The surface density of the Pt{111} face is  $1.5 \times 10^{15}$  atoms·cm<sup>-2</sup> and, thus, this figure can be expressed as 0.028 methyl pyruvate molecules per Pt atom. For the monolayer, the surface coverage was calculated as corresponding to  $2.8 \times 10^{14}$  atoms·cm<sup>-2</sup> ( $\pm 5\%$ ) which can be written as  $7.0 \times 10^{13}$  molecules·cm<sup>-2</sup> ( $\pm 5\%$ ) or 0.047 methyl pyruvate molecules per Pt atom. Similar values for the surface coverage were obtained from an identical calculation using the O(1s) XPS data in both cases (Figure 2(b)). Figures 2(a) and (b) clearly indicate that the C(1s) and O(1s) spectra corresponding to the methyl pyruvate monolayer adsorbed at 298 K do not change during the collection of the NEXAFS data. Therefore effects due to beam-induced decomposition, fragmentation or desorption appear to have been insignificant.

The submonolayer and monolayer C(1s) and O(1s) XP spectra data indicate that the chemical composition of the adsorbate is similar to that in the multilayer. However there are significant differences. In the submonolayer and monolayer regimes, the ratio of the integrated intensities of the two C(1s) features is  $C_{\text{carbonyl}}:C_{\text{alkyl}} = 1.79 \pm 0.05$  (in contrast to  $C_{\text{carbonyl}}:C_{\text{alkyl}} = 1$  observed for the multilayer). Also, the ratio  $C_{\text{total}}:O_{\text{total}}$  is now  $1.47 \pm 0.05$  (as opposed to  $1.29 \pm 0.05$  in the multilayer).

This suggests that at 298 K adsorption of methyl pyruvate into the contact layer results in loss from the surface of an alkyl carbon atom and an oxygen atom, most likely as  $-OCH_x$ . Such  $-OCH_x$  species are known to decompose to CO(a) and H(a) on Pt{111} at 298 K,<sup>28</sup> which are no longer present as surface species. Consistent with this, the characteristic  $\pi^* \text{ C K-edge}$

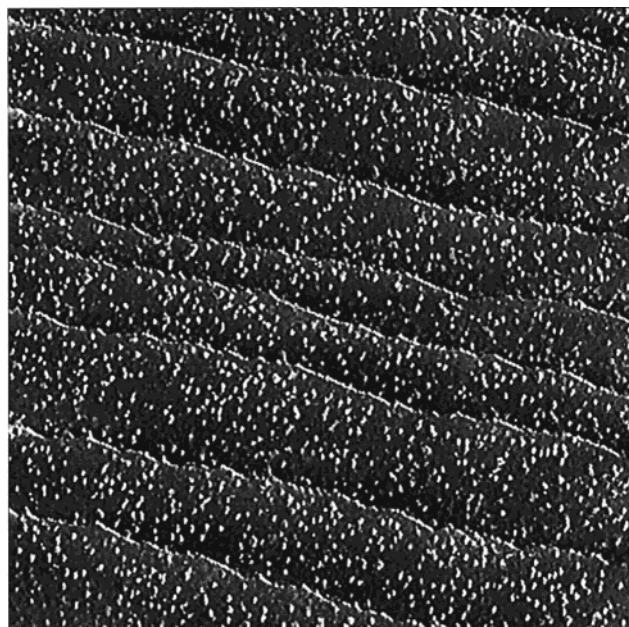


**Figure 3.** STM image (raw data) of methyl pyruvate on Pt{111} at 298 K in the presence of a background pressure of  $2 \times 10^{-5}$  mbar hydrogen. [Constant current mode,  $1000 \text{ \AA} \times 1000 \text{ \AA}$ ,  $U_{\text{gap}} = -1 \text{ V}$ ,  $I_T = 10 \text{ nA}$ ].

resonance for CO on Pt{111} at 288 eV<sup>29</sup> is absent from the methyl pyruvate monolayer spectrum (section 3.3). Thus the multilayer data are consistent with the presence of methyl pyruvate molecules, whereas in the contact layer the chemical state of the adsorbate is altered. We shall now see that this alteration corresponds to polymerization of the pyruvate.

**3.2. Scanning Tunneling Microscopy.** STM images for monolayer coverages of methyl pyruvate were taken at room temperature, in the presence and absence of coadsorbed hydrogen. Recall that hydrogen is the other reactant in the enantioselective reaction of interest. (It was not possible to carry out XPS or NEXAFS (section 3.3) measurements in the presence of a standing pressure of hydrogen while in-beam, due to restrictions on base pressure imposed by the synchrotron facility.)

The “with hydrogen” results were acquired by first dosing the clean surface with hydrogen, then pyruvate, and finally imaging in a standing pressure of  $2 \times 10^{-5}$  mbar H<sub>2</sub>. This procedure ensured that all “non-pyruvate” Pt sites were always saturated with H adatoms. It is apparent from Figure 3 that in the presence of H<sub>a</sub>, methyl pyruvate monomers are distributed uniformly on the terraces of the Pt{111} surface. Identification of these species as monomers is provided by the measured molecular dimensions ( $8 \pm 1 \text{ \AA} \times 3 \pm 0.5 \text{ \AA}$ ) which accord well with the van der Waals dimensions of methyl pyruvate. Thus, in the presence of coadsorbed hydrogen the reactant molecule retains its integrity and the whole of the metal surface should be available for catalytic turnover. No long-range order is apparent, although there is a tendency for the molecules to accumulate at the step edges.

In the absence of coadsorbed hydrogen the picture is very different, as illustrated in Figures 4 (a) and (b). The monomers have undergone reaction yielding mostly linear polymeric structures, although some also exhibit dendritic features. These polymeric species can be up to  $\sim 320 \text{ \AA}$  long ( $\sim 40$  monomer units) and are uniformly distributed over the Pt{111} terraces. No step decoration is apparent. Measurements indicate that the average chain length of these polymers is  $9 \pm 1 n$  units, where



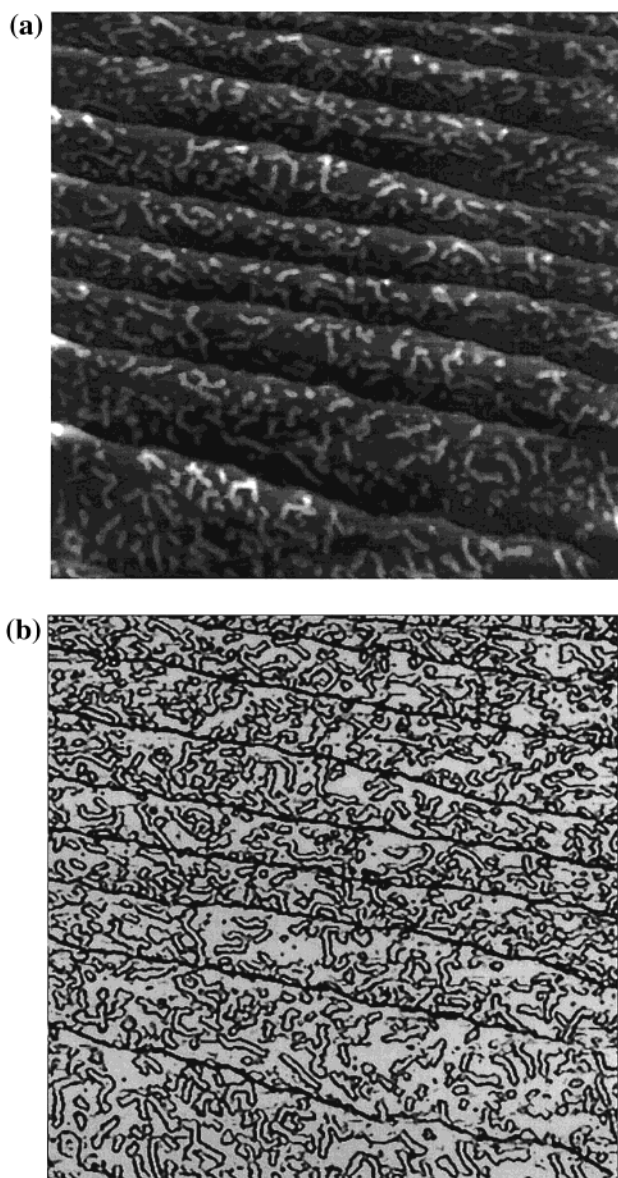


**Figure 4.** (a) STM image (raw data) of methyl pyruvate on Pt{111} at 298 K in the absence of hydrogen showing the formation of polymeric chains [Constant current mode,  $1000 \text{ \AA} \times 1000 \text{ \AA}$ ,  $U_{\text{gap}} = -1\text{V}$ ,  $I_{\text{T}} = 10\text{nA}$ ]. (b) As in (a), but with edge contrast enhanced.

$n$  is the number of monomer units. In this particular case, only about half the initially available Pt sites would be available for catalytic turnover.

Polymerization of aldehydes and ketones on platinum group metals has been noted before,<sup>30–32</sup> although reaction mechanisms have not been discussed in detail. Two plausible mechanisms that cover the present case are shown in Figures 5(a) and (b). Both are aldol condensations: (a) proceeds by elimination of hydrogen and a methoxy species, which decomposes to CO(a) and H(a) at 298 K; (b) proceeds via elimination of hydrogen and water. However, mechanism (b) results in the formation of C=C bonds in the polymeric chains whereas the NEXAFS spectra of the polymer clearly show that such bonds are not present (section 3.3). We therefore discount (b). Mechanism (a) involves initial attack at the ester carbonyl (the most electron deficient center). Once the first “dimer” is produced, the most acidic proton lies in the middle of the resulting molecule: this provides the possibility of subsequent chain growth taking place either linearly or in a branching fashion, in accord with the STM data shown in Figures 4(a) and (b). Furthermore, the resulting

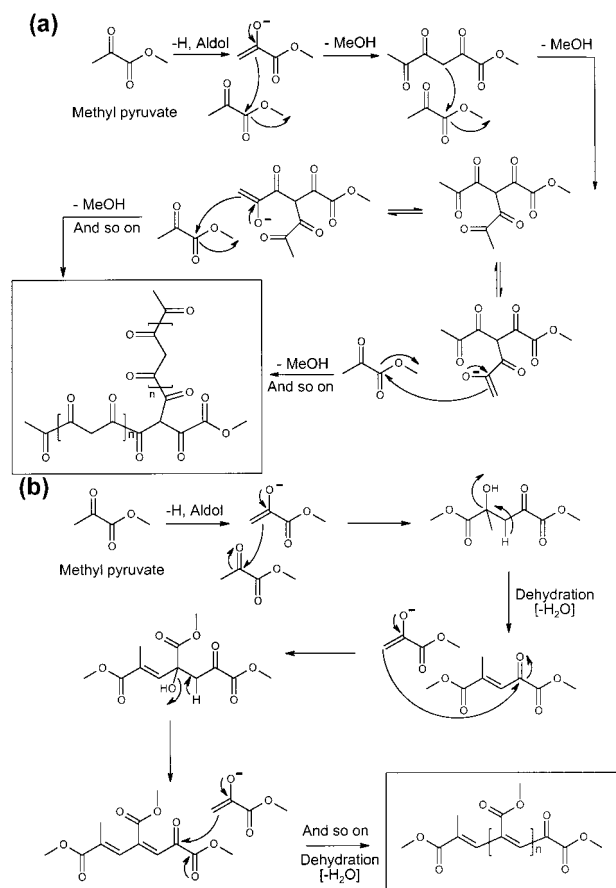


**Figure 5.** Proposed mechanism for methyl pyruvate polymerization on Pt{111} and resulting polymeric structures.

polymeric structures contain only the C=O function, which is in excellent agreement with our NEXAFS data. Our results indicate that under certain conditions self-condensation of the  $\alpha$ -ketoester can be an important unwanted reaction in the enantioselective hydrogenation of methyl pyruvate on Pt surfaces. This reaction occurs in the absence of the chiral modifier when the amount of H(a) is too low. How does coadsorbed hydrogen prevent polymerization? Most likely, this is due to the blocking of adsorption sites which inhibits the first step in the self-condensation reaction (loss of a hydrogen atom by the keto-methyl group (Figure 5)).

A good check on the validity of our model is obtained by correlating the XPS and STM results. As mentioned above, the latter yield a value of  $9 \pm 1$   $n$  monomer units for the average chain length in the polymer. For a linear polymer (the STM images are dominated by linear structures) the  $C_{\text{carbonyl}}:C_{\text{alkyl}}$  ratio is equal to

$$\frac{C_{\text{carbonyl}}}{C_{\text{alkyl}}} = \frac{2 + 2n}{2 + n} \quad (1)$$

and the  $C_{\text{total}}:O_{\text{total}}$  ratio is given by

$$\frac{C_{\text{total}}}{O_{\text{total}}} = \frac{4 + 3n}{3 + 2n} \quad (2)$$

where  $n$  is the number of monomer units. For  $n \rightarrow \infty$ , the  $C_{\text{carbonyl}}:C_{\text{alkyl}}$  is 2 (eq 1), and the  $C_{\text{total}}:O_{\text{total}}$  ratio is 1.5 (eq 2). From XPS, the experimentally determined ratios are  $1.79 \pm 0.05$  and  $1.47 \pm 0.05$ , respectively. Substituting these values into eq 1 and eq 2 yields values for the average linear polymer

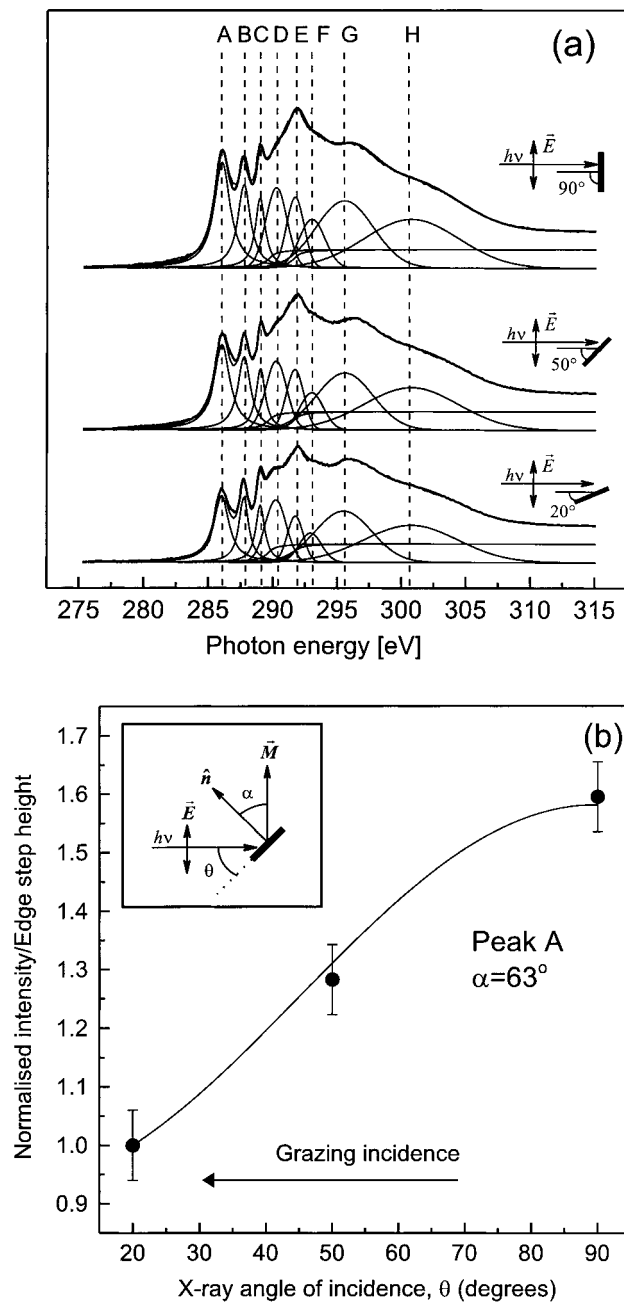


**Figure 6.** (a) Carbon K-edge NEXAFS spectra for multilayer methyl pyruvate on Pt{111} at 95 K and 20°, 50°, and 90° incidence photons. Peaks A, B, and C are  $\pi^*$  resonances and peaks G and H represent  $\sigma^*$  transitions. (b) Plots of the normalized resonance intensities for peaks A and B obtained from fits of the original spectra for multilayer methyl pyruvate on Pt{111} at 95 K.

chain length of  $8 \pm 1$  monomer units and  $7 \pm 2$  monomer units. These values are in good agreement with one another and, moreover, they accord very well the STM result (9 monomer units). The NEXAFS data discussed below corroborate these observations.

**3.3. Near Edge X-ray Absorption Fine Structure, NEXAFS.** **3.3.1 Multilayer C K-edge NEXAFS spectra at 95 K.** Carbon K-edge 95K multilayer NEXAFS spectra (Figure 6(a)) were acquired to assist with the interpretation of the corresponding monolayer spectra taken at 298 K (Figure 7(a)). Methyl pyruvate has two  $\pi^*$  orbitals, denoted  $\pi_1^*$  and  $\pi_2^*$ , which arise from the two C=O bonds present in the molecule. The splitting of the  $\pi$  system is a consequence of conjugation. In a perturbation treatment both “localized” double bonds have

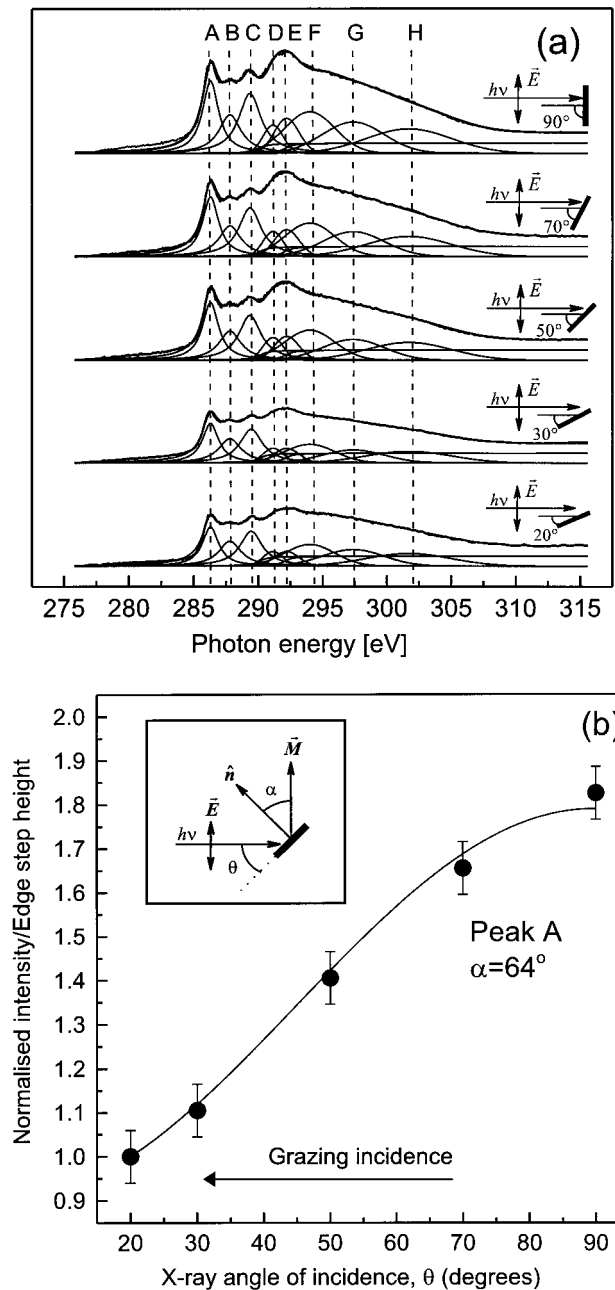


**Figure 7.** (a) Carbon K-edge NEXAFS spectra for a monolayer methyl pyruvate on Pt{111} at 95 K and 20°, 30°, 50°, 70°, and 90° incidence photons. Peaks A, B, and C are  $\pi^*$  resonances and peaks G and H represent  $\sigma^*$  transitions. (b) Plots of the normalized resonance intensities for peaks A and B obtained from fits of the original spectra for a monolayer of methyl pyruvate on Pt{111} at 298 K.

identical  $\pi^*$  antibonding orbitals and the splitting is caused by the first order bond-bond interaction between the two energetically degenerate C=O double bond orbitals. For gaseous ethyl pyruvate, a structurally similar molecule, the energy separation calculated for these two  $\pi^*$  states is of 1.8 eV.<sup>18</sup> Consequently, we would expect strong transitions from the C(1s)<sub>2</sub> and C(1s)<sub>3</sub>, as labeled in Figure 1, to both  $\pi_1^*$  and  $\pi_2^*$  giving rise to four C(1s)  $\rightarrow \pi^*$  transitions at the carbon K-edge. As discussed below, however, only three of these are resolved.

The NEXAFS spectrum (Figure 6(a)) is characterized by eight main features at 286.0 eV (A), 287.7 eV (B), 289.0 eV (C), 290.3 eV (D), 291.8 eV (E), 293.1 eV (F), 296.6 eV (G), and 301.4 eV (H). The most pronounced resonances are the lowest energy peaks A, B, and C. These correspond to

$C(1s) \rightarrow \pi^*(C=O)$  bound-state transitions which lie below the  $C(1s)$  ionization energy, as expected. The energy positions of these resonances compare well with those of the corresponding features observed in the gas-phase in-situ XANES spectra reported for ethyl pyruvate.<sup>18</sup> The resonance at 286.0 eV (peak A) is characteristic of an ester or carboxylic carbon atom and compares favorably with that for the corresponding  $C(1s) \rightarrow \pi^*(C=O)$  transition in formaldehyde at 286.0 eV, in acetaldehyde at 286.3 eV and in acetone at 286.8 eV.<sup>33</sup> It is therefore assigned to the  $C(1s)_2 \rightarrow \pi_1^*(C=O)$  transition. Peak B at 287.7 eV is separated from peak A by 1.7 eV, which corresponds to the energy difference between  $\pi_1^*$  and  $\pi_2^*$  levels. Furthermore, curve fitting shows that it has a similar line-shape and angular dependence to peak A, and on this basis it is assigned to the  $C(1s)_2 \rightarrow \pi_2^*(C=O)$  transition.

The difference in electron binding energy for  $C(1s)_3$  and  $C(1s)_2$  is  $1.4 \text{ eV} \pm 0.1 \text{ eV}$  (measured from the  $C(1s)$  XP spectra in Figure 2(a)), in agreement with the expected value of  $\sim 1.5 \text{ eV}$ .<sup>26</sup> Consequently, the corresponding  $C(1s)_3 \rightarrow \pi_1^*(C=O)$  transition overlaps with the  $C(1s)_2 \rightarrow \pi_2^*(C=O)$  transition and contributes to peak B. Equivalently, the  $C(1s)_3 \rightarrow \pi_2^*(C=O)$  transition is expected at  $\sim 1.4 \text{ eV}$  above  $C(1s)_2 \rightarrow \pi_2^*(C=O)$  and is therefore assigned to peak C (289 eV).

The region containing features C, D, E, and F is congested because it contains the edge-steps as well as discrete resonances. Consequently, a detailed assignment of these spectral features is complicated. Typically, this region between the  $\pi^*$  resonances and the ionization energy in inner shell X-ray absorption spectra is characterized by several sharp but weak resonances. These correspond to excitations to Rydberg orbitals or, in the presence of bonds to hydrogen atoms, to a mixture of Rydberg and hydrogen-derived antibonding orbitals of the same symmetry.<sup>34</sup> The  $3p \pi^*(C-H)$  transition associated with the  $C-CH_3$  group ( $C_1$ ) in methyl pyruvate, similarly to acetaldehyde, is expected around 289.5 eV and, thus, it contributes to peak C. Similar  $C-H^*$  resonances originating from  $O-CH_3$  groups are expected to be chemically shifted to higher energy as in methyl formate and methanol.<sup>35</sup> Therefore, we assign peak D at 290.3 eV to a  $3p \pi^*(C-H)$  transition that arises from the  $O-CH_3$  group ( $C_4$ ) in methyl pyruvate.

Above the ionization energy, the multilayer spectrum exhibits two prominent resonances at 291.8 eV (E) and 293.1 eV (F), and two broader resonances at 296.6 eV (G) and 301.4 eV (H). All represent continuum resonances arising predominantly from  $C(1s) \rightarrow \sigma^*(C-C)$ ,  $C(1s) \rightarrow \sigma^*(C-O)$ , and  $C(1s) \rightarrow \sigma^*(C=O)$  transitions. Such resonances occur widely in the NEXAFS spectra of both saturated and unsaturated organic molecules containing  $C-C$  and  $C-O$  bonds.<sup>22,36</sup> Resonance E at 291.8 eV is assigned to  $C(1s) \rightarrow \sigma^*(C-C)$ . This transition is commonly encountered as the result of  $\sigma^*$  bond-bond interactions in saturated alkyl chains, which are present in both the methyl pyruvate monomer and polymer. Resonance F at 293.1 eV is assigned predominantly to the  $C(1s)_4 \rightarrow \sigma^*(C-O)$  transition. The broad maximum at 296.6 eV (G) is due to  $C(1s)C=O \rightarrow \sigma^*(C-O)$  and is therefore assigned to  $C(1s)_2 \rightarrow \sigma^*(C-O)$  and  $C(1s)_3 \rightarrow \sigma^*(C-O)$  transitions. Resonance H at 301.4 eV corresponds to the transitions for  $C(1s)_2 \rightarrow \sigma^*(C=O)$  and  $C(1s)_3 \rightarrow \sigma^*(C=O)$ .

**3.3.2. Monolayer C K-Edge NEXAFS Spectra at 298 K.** Monolayer NEXAFS spectra recorded at 298 K are shown in Figure 7(a). Eight main features are discernible at 286.3 eV (A), 287.8 eV (B), 289.4 eV (C), 291.2 eV (D), 292.2 eV (E), 294.0 eV (F), 295.9 eV (G), and 300.5 eV (H). A comparison with the multilayer spectra permits the following general

**TABLE 1: Assignment of the Carbon K-edge NEXAFS Resonances for Methyl Pyruvate Multilayer Spectra at 95 K and Monolayer Spectra at 298 K on Pt{111}**

feature	energy $\pm 0.5 \text{ eV}$ multilayer at 95 K	energy $\pm 0.5 \text{ eV}$ monolayer at 298 K	assignment (final orbital)
A	286.0	286.3	$C(1s)_2 \rightarrow \pi_1^*(C=O)$
B	287.7	287.8	$C(1s)_2 \rightarrow \pi_2^*(C=O)$ $C(1s)_3 \rightarrow \pi_1^*(C=O)$
C	289.0	289.4	$C(1s)_3 \rightarrow \pi_2^*(C=O)$ $C(1s)_1 \rightarrow 3p \pi^*(C-H)$
D	290.3	291.2	$C(1s)_4 \rightarrow 3p \pi^*(C-H)$
E	291.8	292.2	$C(1s) \rightarrow \sigma^*(C-C)$
F	293.1	294.0	$C(1s)_4 \rightarrow \sigma^*(C-O)$
G	296.6	295.9	$C(1s)_{2,3} \rightarrow \sigma^*(C-O)$
H	301.4	300.5	$C(1s)_{2,3} \rightarrow \sigma^*(C=O)$

observations. The energy separation of the most prominent  $\pi^*$  and  $\sigma^*$  resonances (A, B and C; F and G) are very similar in the multilayer and monolayer: 1.7 eV, 1.3 eV, 4.8 eV and 1.5 eV, 1.6 eV, 4.6 eV respectively. Curve fitting shows that these resonances have similar line-shape and angular dependence and they are therefore assigned to the corresponding transitions.

However, the width of the  $\pi^*$  resonances in the multilayer are sharper than in the monolayer, reflecting the reduced lifetime of the excited state in the latter case. Also, in the monolayer, resonances are broadened because of the range of different carbon environments present in the polymer. This is a known characteristic of the NEXAFS spectra of polymers that are structurally related to the present case, e.g. polymethylmethacrylate versus its monomer, methyl formate.<sup>35,37</sup>

Note that in the monolayer, the intensity of the Rydberg/ $C-H$  structures associated with the  $O-CH_3$  group (peak D) is significantly reduced. One expects pure Rydberg resonances to be quenched upon chemisorption, whereas the hydrogen-derived resonances should be less attenuated. The much-reduced intensity of peak D is, therefore, consistent with the loss of the  $O-CH_3$  from the molecule, *which is required for polymerization to occur* according to our proposed scheme. Additionally, peak B is dramatically reduced due to: (i) loss of the conjugation in the repeating unit in the polymeric molecules and, hence, a decrease in the number of  $C(1s)_2 \rightarrow \pi_2^*(C=O)$  transitions; and (ii) a reduction of  $C(1s)_3 \rightarrow \pi_1^*(C=O)$  due to the loss of the associated ester moiety ( $C_3$ ) of methyl pyruvate upon polymerization, as proposed. The latter proposition is also in agreement with the reduced intensity of the  $C(1s)_4 \rightarrow \sigma^*(C-O)$  transition. The assignment of resonances is summarized in Table 1.

It is important to note the clear absence of any  $\pi^*$  resonances associated with transitions to  $C=C$  orbitals, typically found around 284 eV.<sup>22</sup> This corroborates further our proposed polymerization mechanism and resulting polymeric structure.

**3.3.3. Molecular Orientation.** The angular dependence of the  $\pi^*$  resonances at the C K-edge for the methyl pyruvate multilayer at 95 K and monolayer at 298 K are shown in Figures 6(b) and 7(b), respectively. To obtain the molecular orientations, the data were normalized following established procedure described in full elsewhere.<sup>22</sup> In Figures 6(a) and 7(a), the bold lines represent the raw data and the lighter lines are deconvolutions of the spectra represented by symmetric Lorentzian and symmetric Gaussian functions for the  $\pi^*$  and  $\sigma^*$  transitions, respectively. A step function was used in fitting the continuum edge step. The insets in Figures 6(b) and 7(b) show the geometry of the experiment;  $\hat{M}$  denotes the normal to the molecular plane and  $\hat{n}$ , the surface normal.

In the multilayer, the molecular orientation determined from the variation in the  $\pi^*$  intensity associated with peak A, as a function of photon incidence angle,  $\theta$ , is of  $63^\circ \pm 5^\circ$  with respect to the metal surface ( $27^\circ \pm 5^\circ$  with respect to the surface



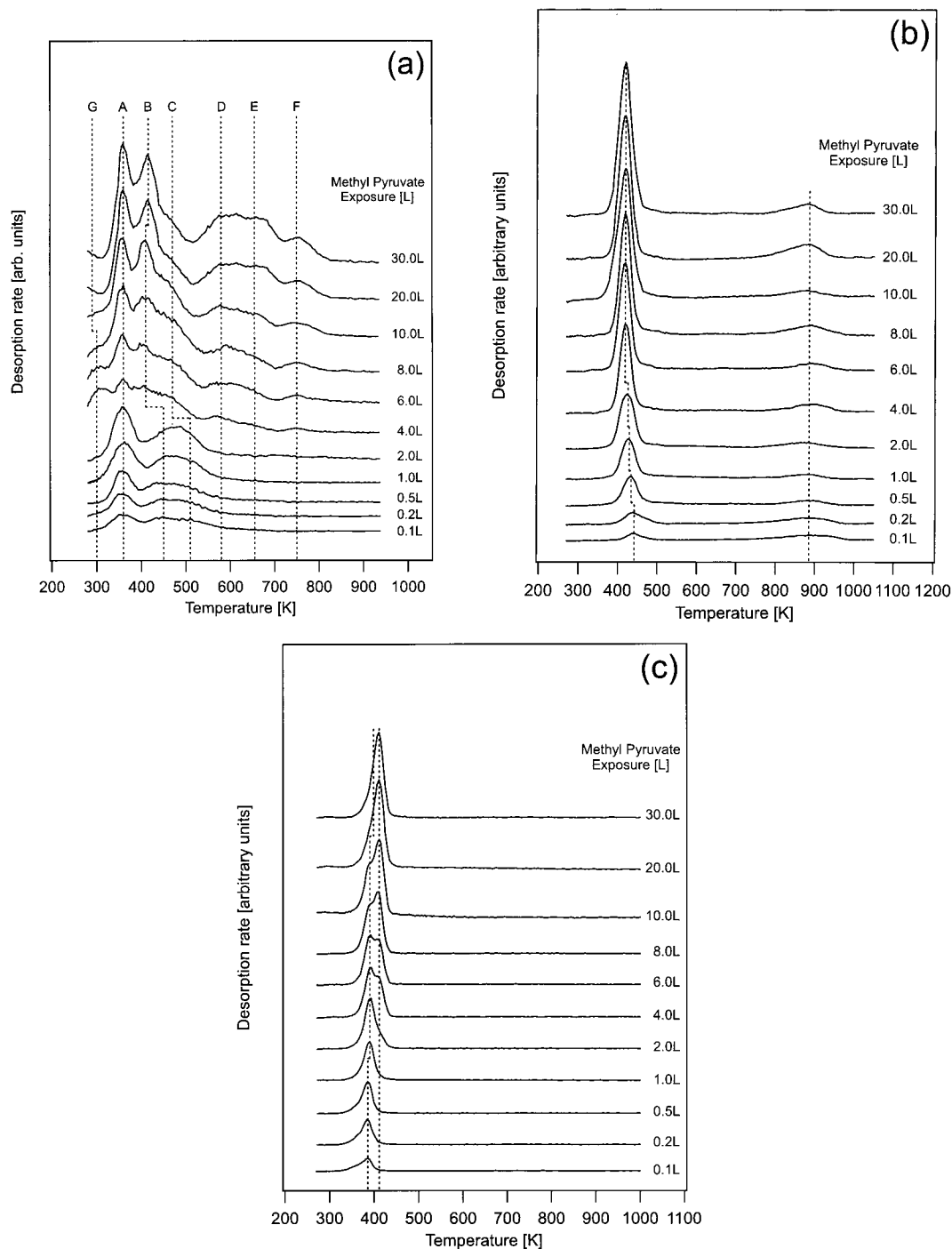


**Figure 8.** Methyl pyruvate TPR spectra on Pt{111}: (a) H<sub>2</sub> desorption; (b) CO desorption; and (c) CO<sub>2</sub> desorption.

normal). This is indicative of a nonrandom arrangement of methyl pyruvate molecules in the multilayer ice.

In the monolayer at 298 K, the C=O bonds form an angle of  $64^\circ \pm 5^\circ$  with respect to the metal surface. Long chain alkanes which lie parallel to metal surfaces in order to maximize the van der Waals interaction, are more weakly bound to metal surfaces than similar molecules bound to the same surface via oxygen lone pairs e.g., alcohols, ethers, aldehydes, and ketones.<sup>38,39</sup> The strongly tilted C=O bonds ( $64^\circ \pm 5^\circ$ ) suggest that the methyl pyruvate polymer is bound to the surface predominantly through the carbonyl oxygen lone pairs. That is, the alkyl backbone is held arched above the surface by the C=O bonds. This upright geometry contrasts with a side-on, flat lying geometry that typically arises in  $\pi$  conjugated systems

and that, in the case of present adsorbate, would be associated with  $\pi$ -bonding via the C=O  $\pi$  system.<sup>40</sup>

**3.4. Temperature Programmed Reaction.** The thermal behavior of adsorbed methyl pyruvate provides useful auxiliary information. The TPR spectra shown in Figure 8 (a)–(c) indicate that at saturation coverage the principal desorption products were CO, H<sub>2</sub>, CO<sub>2</sub>. Smaller quantities of H<sub>2</sub>O and CH<sub>4</sub> were also detected, the relative amounts being CO:H<sub>2</sub>:CO<sub>2</sub>:H<sub>2</sub>O:CH<sub>4</sub>  $\sim$  30:21:12:1:1, after correcting for the mass spectrometer sensitivity. At this coverage, the ratio  $\sim$ 2:1 in respect of the amounts of CO and CO<sub>2</sub>:H<sub>2</sub> evolved, reflects the stoichiometry of the  $n$  repeating unit in the polymer backbone. Saturation coverage is reached at  $\sim 8.3 \times 10^{13}$  ( $\pm 5\%$ ) molecules of methyl pyruvate  $\cdot \text{cm}^{-2}$ . The onset for the polymerization reaction occurs

at  $\sim 1.6 \times 10^{13}$  ( $\pm 5\%$ ) molecules of methyl pyruvate $\cdot\text{cm}^{-2}$ . This is especially clear from the  $\text{H}_2$  desorption spectra in Figure 8(a).

The hydrogen data exhibit multiple features: the principal desorption maximum at  $\sim 360$  K (peak A), is followed by a series of smaller maxima up to 750 K (peaks B–F). Such behavior is commonly observed during the dehydrogenation of alcohols, ethers and esters on Pt{111}.<sup>41</sup>

The main peak (A) is due to the well-known H(a) recombination reaction.<sup>42</sup> The higher temperature peaks are due to stepwise decomposition of organic residues. On Pt{111},  $\text{C}_4$ ,  $\text{C}_3$ , and  $\text{C}_2$  alkylidynes decompose in the temperature range 350–500 K<sup>43</sup> yielding TPR peaks coincident with peaks B and C observed here. Such alkylidynes could arise from the extended alkyl carbon backbone chain of the methyl pyruvate polymer. The small amount of methane detected at 360–500 K could result from the recombination reaction  $\text{CH}_3(\text{a}) + \text{H}(\text{a}) \rightarrow \text{CH}_4(\text{a})$ . Figure 8(a) clearly shows that these features are only present in the  $\text{H}_2$  desorption spectra above an exposure of  $\sim 4\text{L}$  ( $\sim 2.0 \times 10^{13}$  molecules of methyl pyruvate $\cdot\text{cm}^{-2}$ ). This strongly supports the view that polymerization occurs above a certain coverage threshold. Furthermore, in this coverage regime,  $\text{H}_2$  desorption begins immediately upon exposure to pyruvate at 298 K (peak G). The “tail” at 500–750 K (peaks D, E, and F) may reasonably be attributed to decomposition of CH fragments.<sup>43</sup>

$\text{CO}$  desorption (Figure 8(b)) occurred as a single peak at 440–470 K, depending on the coverage – the normal desorption temperature for  $\text{CO}/\text{Pt}\{111\}$ .<sup>44</sup> We ascribe  $\text{CO}_2$  desorption (Figure 8(c)) to the process  $\text{CO}(\text{a}) + \text{O}(\text{a}) \rightarrow \text{CO}_2(\text{g})$ . Below the polymerization threshold, this occurred as a single peak at  $\sim 360$  K. Above the threshold, a second peak appeared at 395 K, presumably associated with oxidation of polymer fragments. The relatively small amount of  $\text{CO}_2$  formation reflects the limited supply of  $\text{O}(\text{a})$  and the fact that on Pt{111}  $\text{CO}$  desorption is faster than  $\text{CO}$  oxidation, even in the presence of excess  $\text{O}(\text{a})$ .<sup>45</sup>

## Conclusions

(1) In the absence of coadsorbed hydrogen, methyl pyruvate polymerizes at room temperature on Pt{111} yielding polymer chains, partly dendritic, of average length equivalent to  $\sim 9$  monomer units. The strongly tilted  $\text{C}=\text{O}$  bonds ( $64^\circ \pm 5^\circ$ ) suggest that the polymer is bound to the surface predominantly via the oxygen lone pairs.

(2) Polymerization occurs by hydrogen elimination from the monomer followed by an aldol condensation that involves elimination of methanol. The proposed mechanism is in excellent accord with the intramolecular bonding, shape, and reactivity of the polymer deduced from the NEXAFS, STM and TPR results.

(3) Coadsorbed hydrogen completely suppresses polymerization: only monomer units are visible in STM.

(4) Irreversible deactivation during start-up or steady-state operation of Pt catalysts in the enantioselective hydrogenation of alkyl pyruvates can be due to hydrogen starvation which results in polymerization of the prochiral reactant.

**Acknowledgment.** J.M.B. acknowledges the award of a CVCP Overseas Research Studentship and additional support from the Cambridge University Oppenheimer Fund. F.J.W. acknowledges financial support from Fundación YPF, Fundación Antorchas, The British Council, Argentina, and King's College Cambridge. This work was supported in part by the U.K. Engineering and Physical Sciences Research Council under Grant No GR/M76706.

## References and Notes

- (1) Collins, A. N.; Sheldrake, G. N.; Crosby, J. *Chirality in Industry: The Commercial Manufacture and Applications of Optically Active Compounds*; John Wiley: New York, 1995.
- (2) Noyori, R. *Chemtech* **1992**, 22, 366.
- (3) Jannes, G.; Dubois, V. *Chiral Reactions in Heterogeneous Catalysis*; Plenum Press: New York, 1995.
- (4) Blaser, H. U.; Baiker, A. *Handbook of Heterogeneous Catalysis*; Ertl, G., Knötzinger, H., Weitkamp, J., Eds.; VCH Publishers: Weinheim, 1997; Vol. 5, p 2422.
- (5) Webb, G.; Wells, P. B. *Catal. Today* **1979**, 12, 319.
- (6) Izumi, I. *Adv. Catal.* **1983**, 32, 215.
- (7) Hutchings, G. J. *Chem. Commun.* **1999**, 301.
- (8) Baiker, A. *J. Mol. Catal.* **1994**, 150, 329.
- (9) Blaser, H. U.; Jalett, H. P.; Müller, M.; Studer, M. *Catal. Today* **1997**, 37, 441.
- (10) Wells, P. B.; Wilkinson, A. G. *Top. Catal.* **1998**, 5, 39.
- (11) Orito, Y.; Imai, S.; Niwa, S.; Hung, N. G. *J. Synth. Org. Chem. Jpn.* **1979**, 37, 173.
- (12) Niwa, S.; Imai, S.; Orito, Y. *J. Chem. Soc. Jpn.* **1982**, 137.
- (13) Wehrli, J. T.; Baiker, A.; Monti, D. M.; Blaser, H. U. *J. Mol. Catal.* **1989**, 49, 195.
- (14) Simons, K. E.; Meheux, P. A.; Griffiths, S. P.; Sutherland, I. M.; Johnston, P.; Wells, P. B.; Carley, A. F.; Rajumon, M. K.; Roberts, M. W.; Ibbotson, A. *Recl. Trav. Chim. Pays-Bas* **1994**, 113/10, 465.
- (15) Augustine, R. L.; Tanielyan, S. K.; Doyle, L. K. *Tetrahedron Asym.* **1993**, 4, 1803.
- (16) Margitfalvi, J. L.; Tfirst, E. *J. Mol. Catal. A Chem.* **1999**, 139, 81.
- (17) Evans, T.; Woodhead, A. P.; Gutiérrez-Sosa, A.; Thornton, G.; Hall, T. J.; Davis, A. A.; Young, N. A.; Wells, P. B.; Oldman, R. J.; Plashkevych, O.; Vahtras, O.; Argen, H.; Carravetta, V. *Surf. Sci.* **1999**, 436, L691.
- (18) Bürgi, T.; Atamny, F.; Knop-Gericke, A.; Hävecker, M.; Schedel-Niedrig, T.; Schlögl, R.; Baiker, A. *Catal. Lett.* **2000**, 66, 209.
- (19) Bonello, J. M.; Lambert, R. M.; Künzle, N.; Baiker, A. *J. Am. Chem. Soc. Rapid Commun.*, in press.
- (20) Wehrli, J. T.; Baiker, A.; Monti, D. M.; Blaser, H. U. *J. Mol. Catal.* **1989**, 49, 195.
- (21) Wehrli, J. T.; Baiker, A.; Monti, D. M.; Blaser, H. U. *J. Mol. Catal.* **1990**, 61, 207.
- (22) Stöhr, J. *NEXAFS Spectroscopy*; Springer-Verlag: Berlin, 1992.
- (23) Fuggle, J. C.; Mårtensson, N. *J. Electron Spectrosc. Relat. Phenom.* **1980**, 21, 275.
- (24) Briggs, D.; Seah, M. P. *Practical Surface Analysis*, 2nd ed.; Wiley: Chichester, 1990; Vol. 1.
- (25) Baddeley, C. J.; Stephenson, A. W.; Hardacre, C.; Tikhov, M.; Lambert, R. M. *Phys. Rev. B* **1997**, 56, 12589.
- (26) Dilks, A. in *Electron Spectroscopy – Theory, Techniques and Applications*; Brundle, C. R., Baker, A. D., Eds.; Academic Press: London, 1981; p 278.
- (27) Yeh, J. J.; Lindau, I. *Atomic Data and Nuclear Data Tables* **1982**, 32, 1.
- (28) Sexton, B. A. *Surf. Sci.* **1981**, 102, 271.
- (29) Sette, F.; Stöhr, J.; Kollin, E. B.; Dwyer, D. J.; Gland, J. L.; Robbins, J. L.; Johnson, A. L. *Phys. Rev. Lett.* **1985**, 54, 935.
- (30) Madix, R. J.; Yamada, T.; Johnson, S. W. *Appl. Surf. Sci.* **1984**, 19, 43.
- (31) Henderson, M. A.; Zhou, Y.; White, J. M. *J. Am. Chem. Soc.* **1989**, 111, 1185.
- (32) Henderson, M. A.; Mitchell, G. E.; White, J. M. *Surf. Sci.* **1987**, 188, 206.
- (33) Hitchcock, A. P.; Brion, C. E. *J. Electron Spectrosc. Relat. Phenom.* **1980**, 19, 231.
- (34) Robin, M. B. *Higher Excited States of Polyatomic Molecules*; Academic Press: New York, 1973; Vol. 1 and Vol. 3.
- (35) Ishii, I.; Hitchcock, A. P. *J. Electron Spectrosc. Relat. Phenom.* **1988**, 46, 55.
- (36) Kempgens, B.; Köppe, H. M.; Kivimäki, A.; Neeb, M.; Maier, K.; Hergenahm, U.; Bradshaw, A. M. *Surf. Sci.* **1999**, 425, L376.
- (37) Outka, D. A.; Stöhr, J. in *Chemistry and Physics of Solid Surfaces VII*; Vanselow, V. R., Howe, R., Eds.; Springer Series in Surface Science; Springer: Berlin, 1988; Vol. 10.
- (38) Avery, N. R. *Surf. Sci.* **1983**, 125, 771.
- (39) Sexton, B. A.; Hughes, A. E. *Surf. Sci.* **1984**, 140, 227.
- (40) Yamamoto, A. *Organotransition Metal Chemistry: Fundamental Concepts and Applications*; Academic Press: New York, 1986.
- (41) Rendulic, K. D.; Sexton, B. A. *J. Catal.* **1982**, 78, 126.
- (42) Christmann, K.; Ertl, G.; Pignet, T. *Surf. Sci.* **1976**, 54, 365.
- (43) Salmeron, M.; Somorjai, G. A. *J. Phys. Chem.* **1982**, 86, 341.
- (44) McCabe, R. W.; Schmidt, L. D. *Surf. Sci.* **1977**, 65, 189.
- (45) Gland, J. L.; Kollin, E. B. *J. Chem. Phys.* **1983**, 78, 963.